

See discussions, stats, and author profiles for this publication at: <https://www.researchgate.net/publication/366186882>

Investigation of Geometrically Nonlinear Effects in the Aeroelastic Behavior of a Very Flexible Wing

Conference Paper · December 2022

CITATIONS
0

READS
212

2 authors:



Cristina Riso
Georgia Institute of Technology
28 PUBLICATIONS 222 CITATIONS

[SEE PROFILE](#)



Carlos E. S. Cesnik
University of Michigan
331 PUBLICATIONS 10,806 CITATIONS

[SEE PROFILE](#)

Some of the authors of this publication are also working on these related projects:



NSF Center for Unmanned Aircraft Systems - University of Michigan [View project](#)



X-HALE [View project](#)

Investigation of Geometrically Nonlinear Effects in the Aeroelastic Behavior of a Very Flexible Wing

Cristina Riso*

Georgia Institute of Technology, Atlanta, GA, 30332

Carlos E. S. Cesnik†

University of Michigan, Ann Arbor, MI, 48109

This paper investigates geometrically nonlinear effects associated with nonlinear kinematics and follower aerodynamics in the aeroelastic behavior of a very flexible wing in low-speed flow. The test case is the Pazy wing, a benchmark model for geometrically nonlinear studies developed under the Third Aeroelastic Prediction Workshop Large Deflection Working Group. The work builds on a validated low-order model of the Pazy wing that consists of a geometrically nonlinear beam coupled with potential flow thin airfoil theory. Neglecting follower aerodynamics underestimates static deflections by up to 10% while neglecting nonlinear kinematics overestimates them by up to 50%. As deflections increase, curvature effects captured by nonlinear kinematics decrease the natural frequencies associated with torsion and in-plane bending motions, reducing the onset and offset speeds of the wing hump mode flutter mechanism. Neglecting follower aerodynamics widens the hump mode instability region and shifts it at 1–4% higher flow speeds but does not change the flutter frequency and amplitude of post-flutter dynamics. Overall, nonlinear kinematics is the primary geometrical nonlinearity influencing the wing aeroelastic behavior. While follower aerodynamics effects change the deformed shape for a given operating condition, natural frequencies and aeroelastic eigenvalues with and without these effects evolve along the same curves once plotted with the flow speed as an implicit parameter. These results will aid future studies in very flexible wings including other nonlinearities such as stall.

I. Introduction

The push for reducing aviation environmental impacts drives aircraft wing designs toward lighter-weight structures and higher aspect ratios [1]. The resulting very flexible wings experience large deflections under normal loads, questioning the validity of linear aeroelastic models and analysis methods used in production environments [2]. This problem motivates research efforts to formulate, verify, and validate new approaches to analyzing and designing next-generation aircraft.

The Third Aeroelastic Prediction Workshop (AePW3) Large Deflection Working Group (LDWG) is one of the ongoing efforts to advance our predictive capabilities for very flexible wings. The group revolves around an experimental benchmark model for geometrically nonlinear studies in low-speed flow, the Pazy wing [3]. The unique feature of the Pazy wing is its ability to withstand loads causing tip vertical displacements up to 50% of the semispan. This unique feature has enabled static and flutter tests at unprecedented deflections [3, 4], providing a rich experimental database for validating a wide range of computational models [5–11]. The Pazy wing has also been used as a test case for nonlinear aeroelasticity research on gust response [12], model-order reduction and active control [13, 14], uncertainty quantification [15, 16], and other topics.

Flutter tests have shown that the Pazy wing has a hump mode flutter mechanism associated with hysteresis [4], which denotes a subcritical bifurcation. This phenomenon is challenging to predict as it requires fully nonlinear dynamic aeroelastic calculations [17]. Studies based on eigenvalue analyses about static deformed shapes captured the flutter onset, but missed the offset due to neglecting nonlinear dynamic effects [5, 6, 8]. Transient analyses that included geometrical nonlinearities also missed the subcritical behavior, predicting a supercritical one instead [9]. These results strengthen the hypothesis that the subcritical hump mode flutter mechanism is driven by aerodynamic nonlinear effects such as stall [4, 9].

*Assistant Professor, Daniel Guggenheim School of Aerospace Engineering, 275 Ferst Drive NW, AIAA Member, criso@gatech.edu.

†Clarence “Kelly” Johnson Professor, Department of Aerospace Engineering, 1320 Beal Avenue, AIAA Fellow, cesnik@umich.edu.



Fig. 1 Pazy wing benchmark case [3].

With the overarching goal of understanding how different nonlinearities impact very flexible wings, this paper investigates geometrically nonlinear effects in the Pazy wing aeroelastic behavior. The specific objectives of the paper are: *i*) analyze the role of nonlinear kinematics and follower aerodynamics in the wing static aeroelastic response, natural frequencies in deformed shape, and hump mode flutter mechanism (including the post-flutter dynamics), and *ii*) assess how models of different complexity predict these effects. The study expands previous work on the role of different geometrically nonlinear effects [18] by considering a larger deflection range up to 50% semispan and by exploring the complete aeroelastic stability scenario and post-flutter dynamics associated with a hump mode instability.

The work builds on an existing low-order model of the Pazy wing [8, 9]. The model consists of a geometrically nonlinear beam described by a strain-based formulation [19] coupled with unsteady potential flow thin airfoil theory [20] with spanwise-varying aerodynamic coefficients [3]. The model is implemented into the University of Michigan Nonlinear Aeroelastic Simulation Toolbox (UM/NAST) [21], a multidisciplinary framework for modeling, analyzing, and simulating very flexible wings and aircraft. The results presented in this paper cover static, modal, flutter, and post-flutter analyses considering nonlinear or linear kinematics and follower or nonfollower aerodynamics. Results from the low-order model are compared with higher-order numerical solutions where possible.

The remainder of this paper is organized as follows: Sec. II introduces the Pazy wing; Sec. III recalls the computational framework; Sec. IV describes the numerical model; Sec. V discusses the results, and a section of concluding remarks ends the paper.

II. Pazy Wing Benchmark Case

Figure 1 shows the Pazy wing, a public experimental benchmark model for geometrically nonlinear studies in low-speed flow [3]. The wing was developed at the Technion under the AePW3-LDWG effort and has a semispan $\ell = 0.55$ m, a chord $c = 0.1$ m, and a uniform untwisted NACA 0018 cross section. The structure consists of a 7075 aluminum spar, a 3D-printed nylon 12 frame, an Oraling polyester skin, and a 3D-printed tip rod. Reference [3] details the design, ground vibration testing, and the wind-tunnel tests focused on the wing static aeroelastic response and hard flutter crossing mechanism. Reference [4] discusses the second test campaign focused on the hump mode flutter mechanism.

III. Computational Framework

The Pazy wing is analyzed in UM/NAST [21], a low-order multidisciplinary framework to study very flexible wings and aircraft. While no new UM/NAST development was required in this work, the framework is described below to make the paper self-contained and explain the modeling of different geometrically nonlinear effects.

A. Theoretical Formulation

UM/NAST models an aircraft as a set of beams representing different components that undergo arbitrary deflections relative to a body-fixed frame B , in rigid-body motion within an inertial frame G . The B frame position in the G frame is given by the vector p_B , resolved in the B frame, and its orientation is such that the unit vector B_x points downstream, B_y toward the right wingtip, and B_z completes the right-hand triad. The flexible motion is described by local frames w , which origin at points p along each beam member and are oriented such that w_x is along the beam reference axis, w_y is toward the leading edge, and w_z completes the right-hand triad.

The position and orientation of a beam point at a fixed time are given by the 12×1 vector

$$h(s)^T = \{p(s)^T \ w_x(s)^T \ w_y(s)^T \ w_z(s)^T\} \quad (1)$$

The quantity s in Eq. (1) is the curvilinear coordinate along the beam reference axis and p , w_x , w_y , and w_z are 3×1 unit vectors resolved in the B frame. Each beam member is discretized in three-node finite elements with four strain degrees of freedom (DOF): ε_x (axial extension), κ_x (torsion curvature), κ_y (out-of-plane bending curvature), and κ_z (in-plane bending curvature). The deformed configuration h is recovered from the strains as a dependent quantity by space-marching the kinematic relations in Refs. [19, 21].

The UM/NAST equations of motion are [21]

$$\begin{bmatrix} M_{FF} & M_{FB} \\ M_{BF} & M_{BB} \end{bmatrix} \begin{Bmatrix} \ddot{\varepsilon} \\ \dot{\beta} \end{Bmatrix} + \begin{bmatrix} C_{FF} & C_{FB} \\ C_{BF} & C_{BB} \end{bmatrix} \begin{Bmatrix} \dot{\varepsilon} \\ \beta \end{Bmatrix} + \begin{bmatrix} K & 0 \\ 0 & 0 \end{bmatrix} \begin{Bmatrix} \varepsilon \\ b \end{Bmatrix} = \begin{Bmatrix} R_F \\ R_B \end{Bmatrix} \quad (2)$$

$$\dot{\zeta} = -\frac{1}{2} \Omega_\zeta \zeta \quad \dot{P}_B = [C^{GB} \ 0] \beta \quad (3)$$

$$\dot{\lambda} = F_1 \begin{Bmatrix} \ddot{\varepsilon} \\ \dot{\beta} \end{Bmatrix} + F_2 \begin{Bmatrix} \dot{\varepsilon} \\ \beta \end{Bmatrix} + F_3 \lambda \quad (4)$$

The quantity ε is the model strain vector, β is the 6×1 vector of the rigid-body linear and angular velocities of the B frame with respect to the G frame (resolved in the B frame), and b is the 6×1 vector of their time integrals. The quantities $M_{FF} = M_{FF}(\varepsilon)$, $M_{FB} = M_{FB}(\varepsilon)$, $M_{BF} = M_{BF}(\varepsilon)$, and $M_{BB} = M_{BB}(\varepsilon)$ in Eq. (2) are generalized mass matrices; $C_{FF} = C_{FF}(\dot{\varepsilon}, \varepsilon, \beta)$, $C_{FB} = C_{FB}(\dot{\varepsilon}, \varepsilon, \beta)$, $C_{BF} = C_{BF}(\dot{\varepsilon}, \varepsilon, \beta)$, and $C_{BB} = C_{BB}(\dot{\varepsilon}, \varepsilon, \beta)$ are generalized damping matrices; and $K = K_{FF}$ is the constant stiffness matrix of the strain-based formulation [19]. The vectors $R_F = R_F(\ddot{\varepsilon}, \dot{\varepsilon}, \varepsilon, \dot{\beta}, \beta, \zeta, \lambda)$ and $R_B = R_B(\ddot{\varepsilon}, \dot{\varepsilon}, \varepsilon, \dot{\beta}, \beta, \zeta, \lambda)$ in Eq. (2) list the generalized loads for the flexible and rigid-body DOF. The quantity $\Omega_\zeta(\beta)$ in Eq. (3) is the quaternion propagation matrix that relates the 4×1 quaternion vector ζ to its time derivative $\dot{\zeta}$, $C^{GB}(\zeta)$ is the rotation matrix from the B to the G frame, and $P_B := C^{GB} p_B$ is the position of the B frame within the G frame resolved in that frame. The aerodynamic states λ describe wake lags and evolve according to the first-order equations (4) with coefficients given in $F_1 = F_1(\varepsilon)$, $F_2 = F_2(\varepsilon)$, and F_3 .

The framework implements multiple aerodynamic theories such as the potential flow thin airfoil theory of Peters et al. [20]. These theories compute the aerodynamic loads at the cross sections of the beam nodes based on local flow and control parameters such as effective angle of attack, Mach number, and flap deflections. The local parameters are evaluated at the previous numerical iteration or time step and are mapped onto the aerodynamic loads using user-specified airfoil properties, lookup tables, or surrogate models. The aerodynamic loads may be corrected for additional wingtip, sweep, or compressibility effects. No displacement interpolation or load transfer scheme is required because structural and aerodynamic information is exchanged at the beam nodes.

This work uses the UM/NAST static, modal, flutter, and dynamic solvers [21]. The static solver computes the deformed shape under aerodynamic and other applied loads. The modal solver computes the natural frequencies and mode shapes in the undeformed configuration or after a static solution. The flutter solver computes the stability scenario for a range of operating conditions by *i*) solving for the static deformed shape at each operating condition, *ii*) linearizing the equations of motion about each deformed shape to obtain the local state-space matrix, *iii*) extracting the eigenvalues of each state-space matrix, *iv*) and processing the eigenvalues for all the operating conditions to identify instabilities and output root loci or frequency and damping diagrams. The dynamic solver first computes the static deformed shape at a given operating condition and then time-marches the equations of motion to simulate the transient response for given control inputs, gust disturbances, or other time-varying loads.

B. Geometrically Nonlinear Effects

This work investigates geometrically nonlinear effects due to nonlinear kinematics and follower aerodynamic loads. UM/NAST can consider these effects individually or in combination, resulting in four cases: fully nonlinear, nonfollower loads, linear kinematics, and fully linear.

As mentioned in Sec. III.A, UM/NAST uses beam strains as the structural DOF and recovers the deformed shape by space marching the strain-based kinematic equations [19, 21]. These equations are nonlinear by nature so to capture shortening and curvature effects. In the linear kinematics case, the equations are linearized about the undeformed shape such that shortening and curvature effects are neglected. This results in a solution process akin to that used in standard linear finite element solutions (except for using strain DOF). Differently from standard linear aeroelastic solvers, UM/NAST computes and applies the aerodynamic loads in the deformed shape even in the case of linear kinematics.

To explain how UM/NAST accounts for follower aerodynamics, consider the potential flow thin airfoil theory of Peters et al. [20] with user-specified airfoil properties. The local lift, quarter-chord pitching aerodynamic moment, and drag per unit length at a point along the beam reference axis are given by [22]

$$\begin{aligned} l &= \rho b \dot{y}^2 C_{l_\alpha} \alpha_{\text{eff}} + \pi \rho b^2 (-\ddot{z} + \dot{y} \dot{\alpha} - d \ddot{\alpha}) \\ m_{c/4} &= 2 \rho b^2 \dot{y}^2 (C_{m_0} + C_{m_\alpha} \alpha_{\text{eff}}) + \pi \rho b^3 \left[\frac{\ddot{z}}{2} - \dot{y} \dot{\alpha} - \left(\frac{b}{8} - \frac{d}{2} \right) \ddot{\alpha} \right] \\ d &= -\rho b \dot{y}^2 (C_{d_0} + C_{d_\alpha} \alpha_{\text{eff}}) \end{aligned} \quad (5)$$

Equation (5) involves the air density ρ , the local aerodynamic chord $c = 2b$, the airfoil properties C_{l_α} , C_{m_α} , C_{d_α} , C_{m_0} , and C_{d_0} , the elastic center offset d from the quarter chord, the linear velocity components \dot{y} (horizontal, upstream positive) and \dot{z} (vertical, upward positive), the pitch rate $\dot{\alpha}$ (clockwise positive), the linear and angular accelerations \ddot{z} and $\ddot{\alpha}$, and the effective angle of attack [22]

$$\alpha_{\text{eff}} = -\frac{\dot{z}}{\dot{y}} + \left(\frac{b}{2} - d \right) \frac{\dot{\alpha}}{\dot{y}} - \frac{\lambda_0}{\dot{y}} \quad (6)$$

where λ_0 is the zeroth-order term in the inflow expansion [20]

$$\lambda_0 \approx \frac{1}{2} \sum_{i=1}^{N_\lambda} b_n \lambda_n \quad (7)$$

The velocity and acceleration components in Eqs. (5) and (6) are in the local zero-lift aerodynamic frame at the current beam node [22]. In the follower case, the aerodynamic loads in Eq. (5) are defined in the same aerodynamic frame, whose orientation varies with deformation. In the nonfollower case, the aerodynamic loads in Eq. (5) are defined in the body frame such that, for instance, the local force l is always along the unit vector B_z . In either case, the aerodynamic loads are computed and applied in the current deformed shape considering the geometrically nonlinear local effective angle of attack in Eq. (6). Neglecting follower effects thus impacts the solution in the following ways: it misses the changes in the aerodynamic load orientation with deformation and, consequently, results in different magnitude of the loads due to different deformed shapes. This work does not consider the impact of linearizing the local effective angle of attack. Reference [23] reports static aeroelastic results illustrating this aspect.

Because UM/NAST always computes the aerodynamic loads in the deformed shape based on the local effective angle of attack in Eq. (6), the “fully linear” case (linear kinematics and nonfollower aerodynamics) does not exactly reproduce a standard linear aeroelastic solution of off-the-shelf solvers such as MSC Nastran SOL 144 [24]. However, Sec. V.A shows that the differences between a true linear static aeroelastic solution and the fully linear case of this work are slight. In all cases, the local aerodynamic loads per unit length in Eq. (5) are integrated along the span using the undeformed beam element lengths, which prevents nonphysical load magnification due to structural stretching in the presence of linear kinematics.

IV. Low-Order Aeroelastic Model

This work builds on a verified and validated low-order aeroelastic model of the Pazy wing in UM/NAST [8, 9]. The model is described below and its properties are available for download from the authors’ GitHub repository*.

*<https://github.com/UM-A2SRL/AePW3-LDWG.git>

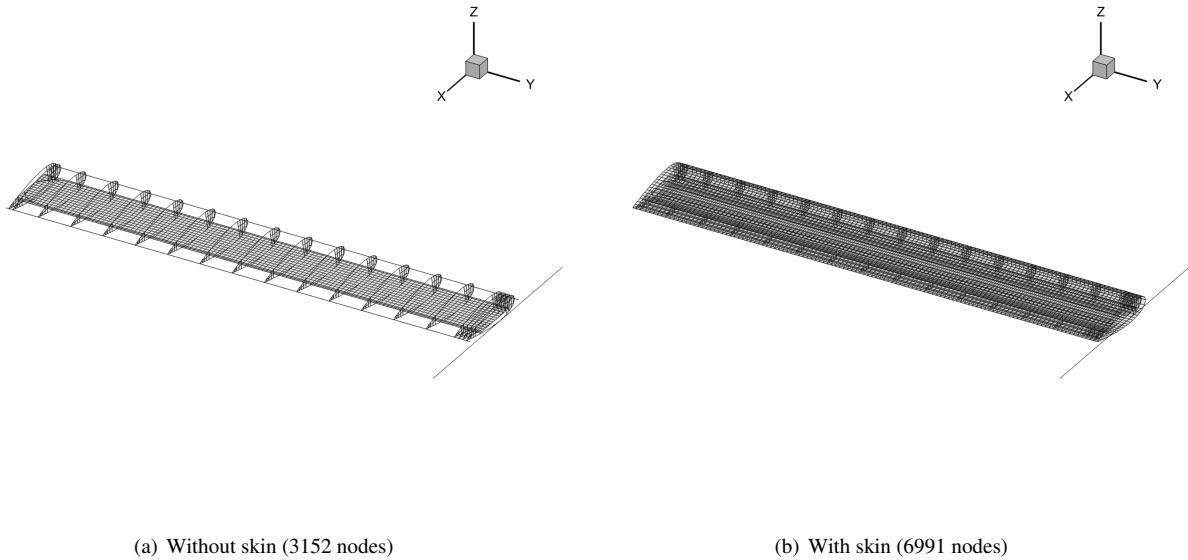


Fig. 2 Pazy wing built-up FEM [8].

Table 1 Pazy wing with skin natural frequencies in undeformed shape.

GVT [3]			SOL 103 [8]			UM/NAST [8]		
#	Mode type	Freq. (Hz)	Mode type	Freq. (Hz)	$\Delta_{\text{Test}} (\%)$	Mode type	Freq. (Hz)	$\Delta_{\text{FEM}} (\%)$
1	OOP1	4.26	OOP1	4.19	-1.58	OOP1	4.19	-0.04
2	OOP2	28.50	OOP2	28.49	-0.02	OOP2	28.49	0.00
3	T1	42.00	T1	41.97	-0.08	T1	41.88	-0.21
4	IP1	60.70	OOP3	82.92	1.74	OOP3	83.06	0.17
5	OOP3	81.50	IP1	104.98	72.95	IP1	105.89	0.87

A. Structural Model

The beam structural model is derived from the built-up finite element model (FEM) in Fig. 2 using the University of Michigan's Enhanced FEM2Stick framework [25]. The reference axis is at 44% chord in the airfoil symmetry plane and is discretized in 15 elements (60 strain DOF). The inertia properties are given by rigid-body elements at the beam nodes with masses, offsets, and inertia tensors derived from the built-up FEM mass matrix. The stiffness properties consist of the elements of the cross-sectional stiffness matrix of the strain-based formulation of Ref. [19]. The stiffness matrix for each beam element has the axial, torsional, and out-of-plane/in-plane bending stiffness constants on the diagonal, while the off-diagonal terms describe coupling effects between strain measures. These quantities are identified for each beam element based on static solutions of the built-up FEM and are constant with structural deflections due to the assumed materially linear stress-strain constitutive relation. The strain-based formulation of Ref. [19] captures geometric stiffening with no stiffness matrix updates required in displacement-based formulations.

The beam model was assessed by comparing modal and static results with solutions for the built-up FEM and experimental data from ground vibration and static tests [8]. The modal comparisons showed that the beam model captures the first five natural frequencies of the Pazy wing with the same accuracy as the built-up FEM (errors below 1%, see Table 1) while requiring up to 700 times fewer DOF. The static comparisons showed that the beam model predicts the same deformed shapes as the built-up FEM over a tip deflection range from 0 to 45% semispan. Beyond requiring much fewer DOF, the beam model is more numerically stable than the built-up FEM, which cannot be used in nonlinear solutions in the version with the skin due to numerical convergence issues.

B. Aerodynamic Model

The Pazy wing low-order aeroelastic model couples the beam model described in Sec. IV.A with the potential flow thin airfoil theory of Peters et al. [20]. The aerodynamic model consists of 15 strips each associated with a beam element (90 aerodynamic DOF in dynamic solutions). Two model variants are available that both implement user-specified airfoil properties independent of the flow conditions but treat wingtip effects in different ways.

The first low-order aerodynamic model [8] features a spanwise-constant flat-plate airfoil and captures wingtip effects using tip loss corrections, which are tuned by matching selected static aeroelastic responses of a higher-order model that couples the beam structure with the vortex-lattice method (VLM) called UM/NAST-VLM model. The second low-order aerodynamic model [9] uses spanwise-variable airfoil properties based on the true Pazy wing aerodynamic geometry. These properties are obtained from a rigid aerodynamic analysis of the wing undeformed shape at root angle of attack $\alpha_r = 1$ deg conducted at the Technion [5] using the ZAERO panel solver [26]. This low-order aerodynamic model does not require higher-order solutions for tip loss tuning, making it preferable for this study that aims to explore different combinations of geometrically nonlinear effects. For this reason, all the results in this paper are obtained using the second low-order aerodynamic model.

The airfoil properties consist of the lift curve slope $C_{l\alpha}$ and the non-dimensional center of pressure position along the chord r_{cp} measured from the leading edge. The quarter-chord pitching aerodynamic moment coefficient derivative for UM/NAST (Fig. 3) is obtained as

$$C_{m\alpha} = -C_{l\alpha} (r_{cp} - 0.25) \quad (8)$$

The aerodynamic coefficient derivatives $C_{l\alpha}$ and $C_{m\alpha}$ are specified in the local zero-lift aerodynamic frame associated with each beam node, and the aerodynamic loads are set to zero at the wing tip.

The complete aeroelastic model was assessed by comparing static and flutter results with higher-order numerical solutions and wind-tunnel experiments [9]. The static aeroelastic comparisons showed that the low-order model captures the Pazy wing deformed shape over a wide range of flow conditions (flow speeds and root angles of attack) within 1.5% of the UM/NAST-VLM model. The low-order model also captures the hump mode flutter onset in deformed shape within 3.5% of the experimental data. The flutter onset in undeformed shape showed larger errors up to 30% compared with a linear flutter analysis of the built-up FEM coupled with the doublet-lattice method (DLM) [9]. This surprising behavior is attributed to the high sensitivity of the hump mode flutter mechanism to small variations in the damping predicted by different unsteady aerodynamic models at low deflections. Geometrically nonlinear effects drive the instability at large deflections, making the hump mode flutter onset less sensitive to differences in unsteady aerodynamic modeling. The discrepancies in predicting the hump mode instability onset in the linear regime are acceptable for the scope of this study that focuses on large deflections.

V. Results

This section analyzes the impact of nonlinear kinematics and follower aerodynamic loads on the Pazy wing aeroelastic behavior. All analyses neglect gravity effects and consider the model with skin unless stated otherwise. Tip displacements are recovered at the midchord point, and tip twist angles are computed from the differential displacements of the tip leading and trailing edges. The static and modal results are obtained with a 0.01 kg mass on the tip rod 0.01 m behind the trailing edge, which is removed in the flutter results to make the hump mode unstable.

A. Static Aeroelastic Response

Figures 4 and 5 show the Pazy wing tip displacements and tip twist angles for flow speed $U = 0 \rightarrow 60$ m/s at the root angles of attack $\alpha_r = 5, 7$ deg. Figure 6 compares deformed shapes for selected conditions [3]: $U = 30$ m/s and $\alpha_r = 5$ deg (Case 1); $U = 50$ m/s and $\alpha_r = 5$ deg (Case 2); $U = 55$ m/s and $\alpha_r = 7$ deg (Case 3). The blue solid lines indicate the fully nonlinear UM/NAST results (nonlinear kinematics and follower aerodynamics); the blue dashed lines and the blue dotted lines with circles show the results obtained considering nonlinear kinematics and nonfollower aerodynamics or linear kinematics and follower aerodynamics, respectively; and the blue dotted lines with crosses indicate the fully linear results (linear kinematics and nonfollower aerodynamics). The figures include fully nonlinear UM/NAST-VLM solutions denoted by purple solid lines, obtained by coupling the beam model with the VLM. Finally, the yellow dotted lines with crosses show the solutions from the MSC Nastran linear static aeroelastic solver SOL 144 [24] obtained by coupling the built-up FEM with the linear VLM. The UM/NAST-VLM and SOL 144 results are included to show how three-dimensional aerodynamic effects impact the solution for different levels of nonlinearity. Reducing the built-up FEM to a beam was found to play only a small role [8, 9].

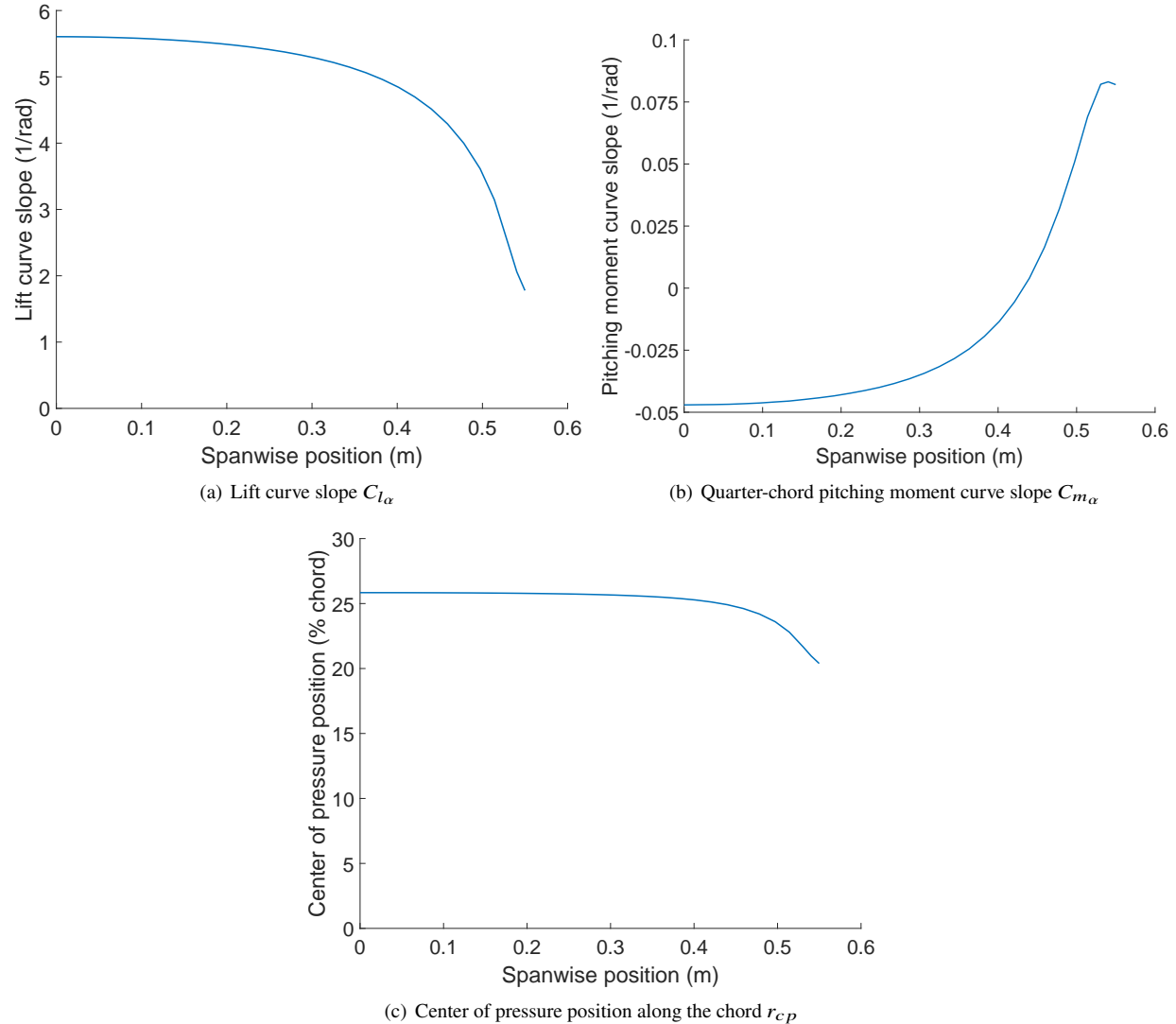


Fig. 3 Pazy wing aerodynamic properties [9].

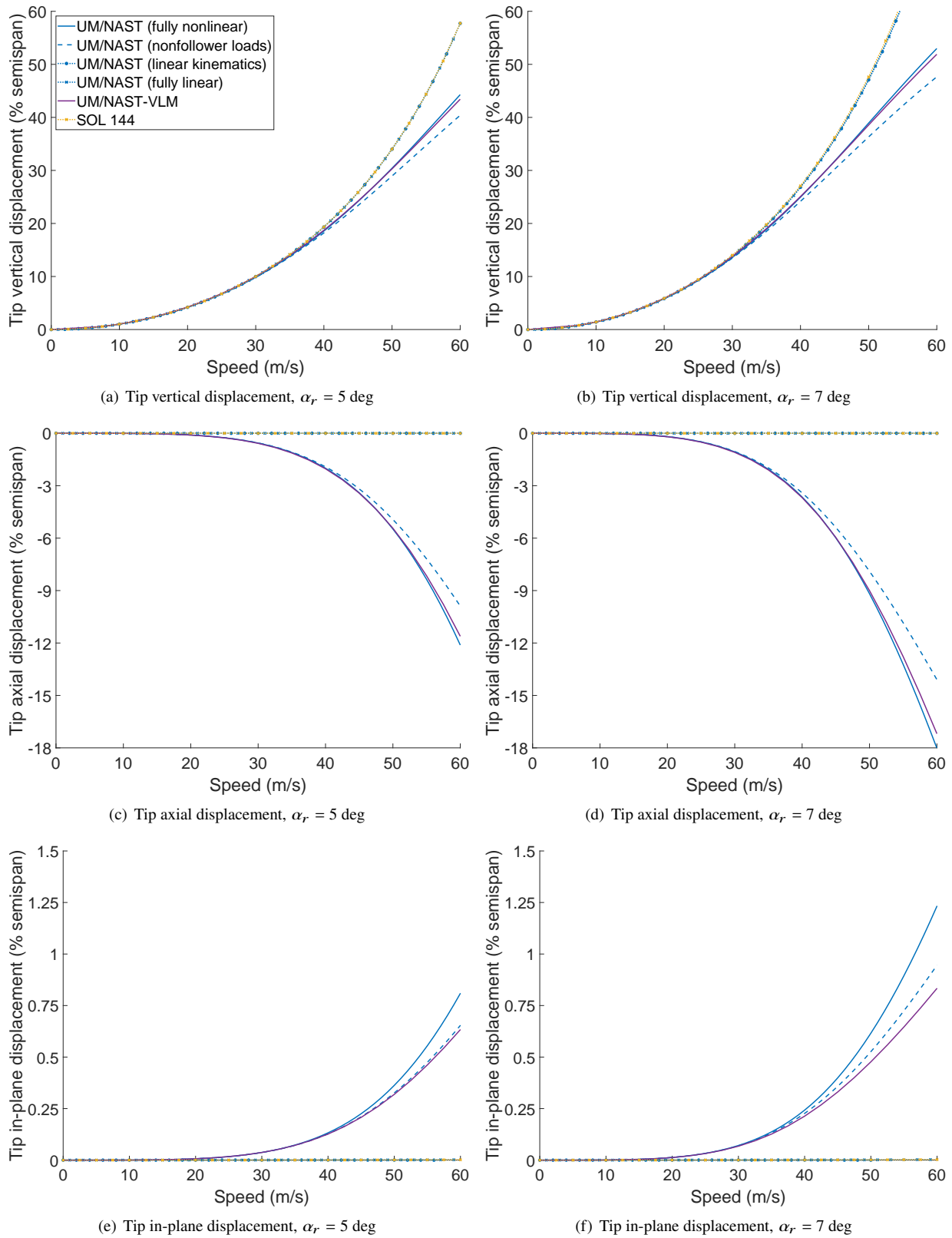


Fig. 4 Pazy wing static aeroelastic tip displacements.

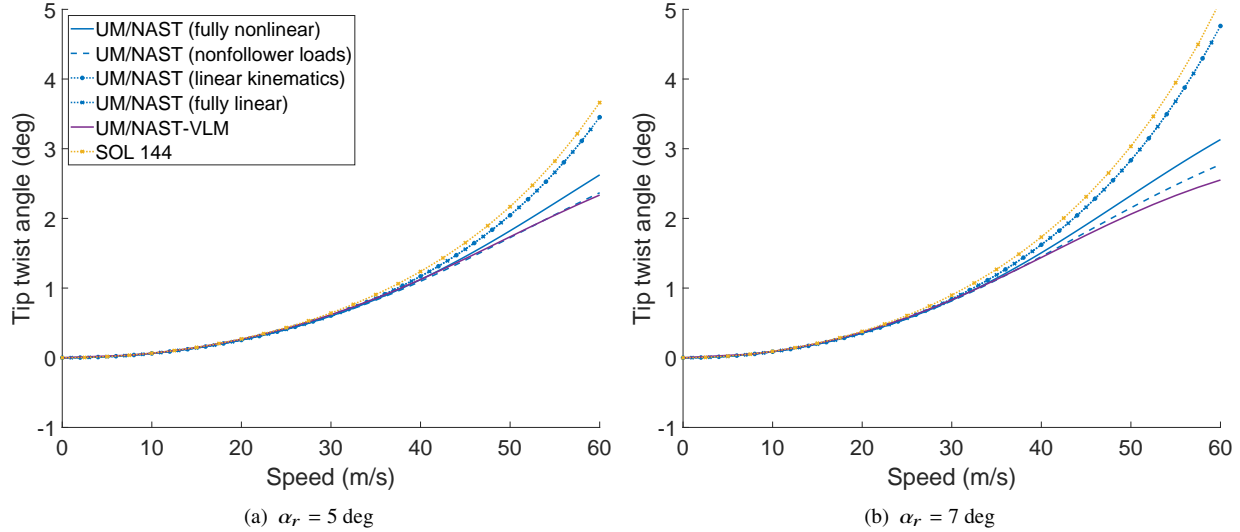


Fig. 5 Pazy wing static aeroelastic tip twist angles.

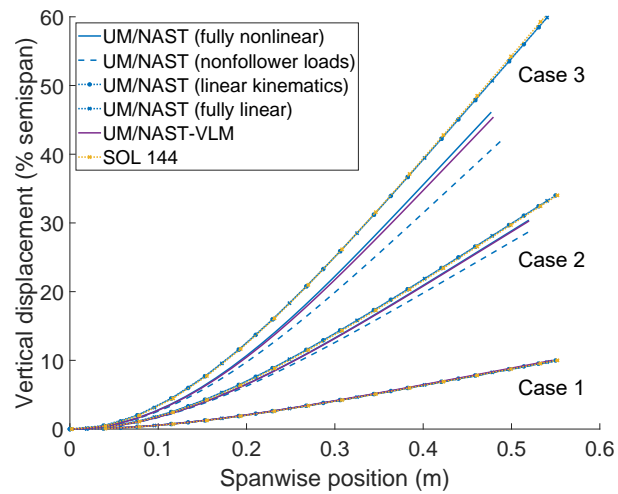


Fig. 6 Pazy wing static aeroelastic deformed shapes for selected conditions.

Table 2 Pazy wing static aeroelastic tip vertical displacements (% semispan) for selected conditions.

(a) $\alpha_r = 5$ deg							
U (m/s)	Fully nonlinear	Nonfollower loads	Δ (%)	Linear kinematics	Δ (%)	Fully linear	Δ (%)
30	9.87	9.82	-0.53	9.98	1.08	9.98	1.07
40	18.57	18.22	-1.90	19.32	3.99	19.31	3.98
50	30.41	28.94	-4.82	34.00	11.80	34.00	11.79
60	44.28	40.39	-8.78	57.72	30.34	57.71	30.33

(b) $\alpha_r = 7$ deg							
U (m/s)	Fully nonlinear	Nonfollower loads	Δ (%)	Linear kinematics	Δ (%)	Fully linear	Δ (%)
30	13.60	13.47	-0.98	13.88	2.06	13.88	2.05
40	24.96	24.18	-3.16	26.82	7.45	26.82	7.43
50	38.92	36.32	-6.69	47.08	20.96	47.08	20.95
60	52.98	47.65	-10.07	79.52	50.08	79.51	50.07

Table 3 Pazy wing static aeroelastic tip twist angles (deg) for selected conditions.

(a) $\alpha_r = 5$ deg							
U (m/s)	Fully nonlinear	Nonfollower loads	Δ (%)	Linear kinematics	Δ (%)	Fully linear	Δ (%)
30	0.60	0.60	-0.61	0.61	1.11	0.61	1.10
40	1.12	1.10	-2.15	1.17	4.12	1.17	4.11
50	1.82	1.72	-5.40	2.05	12.23	2.05	12.22
60	2.62	2.37	-9.77	3.45	31.55	3.45	31.53

(b) $\alpha_r = 7$ deg							
U (m/s)	Fully nonlinear	Nonfollower loads	Δ (%)	Linear kinematics	Δ (%)	Fully linear	Δ (%)
30	0.82	0.82	-1.12	0.84	2.13	0.84	2.12
40	1.51	1.45	-3.59	1.62	7.69	1.62	7.68
50	2.33	2.15	-7.58	2.83	21.72	2.83	21.71
60	3.13	2.77	-11.44	4.76	52.06	4.76	52.05

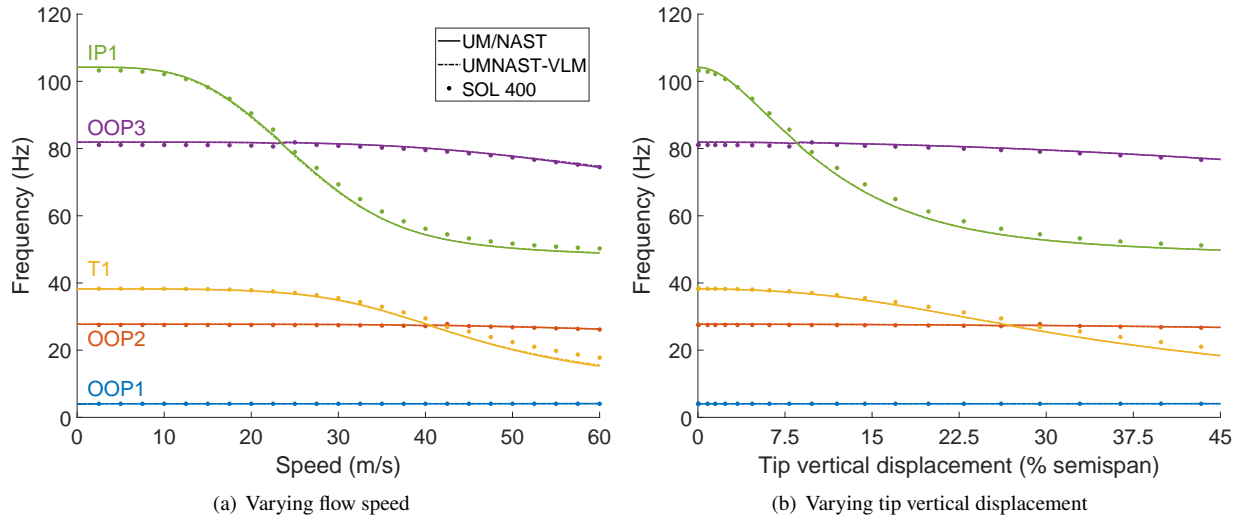


Fig. 7 Verification of Pazy wing modal analysis in deformed shape at $\alpha_r = 7$ deg.

Follower effects play a role as tip vertical displacements exceed 10–15% semispan. Neglecting these effects while keeping nonlinear kinematics (blue dashed lines) gives smaller tip vertical displacements than the fully nonlinear case [Figs. 4(a) and 4(b)]. This is because nonfollower aerodynamic forces do not remain normal to the beam reference axis as the wing deflects, producing an axial component that does not contribute to out-of-plane bending. Smaller tip vertical displacements translate to smaller (in magnitude) axial displacements due to weaker shortening effects [Figs. 4(c) and 4(d)], with slighter impacts on in-plane displacements and twist angles [Figs. 4(e), 4(f), 5(a), and 5(b)].

Nonlinear kinematics also plays a role as tip vertical displacements exceed 10–15% semispan. Assuming linear kinematics with follower aerodynamics (blue dotted lines with circles) severely overestimates tip vertical displacements [Figs. 4(a) and 4(b)] and twist angles [Figs. 5(a) and 5(b)] while it misses other displacement components [Figs. 4(c) to 4(f)]. The deformed shapes based on linear kinematics are significantly stretched and depart from those based on nonlinear kinematics at larger deflections (Case 2 and 3 in Fig. 6). With linear kinematics, follower aerodynamics should give smaller tip vertical displacements for a given condition because aerodynamic loads do not remain normal to the *undeformed* beam reference axis as the wing deflects (linearly). However, the results with and without follower aerodynamics are the same in the case of linear kinematics.

Figures 4 to 6 show that the UM/NAST fully linear results lie on top of the SOL 144 results. Thus, not only the beam model captures the behavior of the built-up FEM [8], but also the low-order aerodynamic model accurately captures steady wingtip effects. These results corroborate previous findings for the fully nonlinear case [8, 9] and verify the UM/NAST linear static aeroelastic capabilities. The agreement between the UM/NAST and SOL 144 fully linear solutions shows that computing the aerodynamic loads in the deformed shape based on the geometrically nonlinear local effective angle of attack has a slight impact on the results. Differences between the fully nonlinear UM/NAST and UM/NAST-VLM results are small but increase with the flow speed. This is because wingtip effects are stronger at larger deflections due to the shorter effective wing semispan. The UM/NAST-VLM model captures this effect because it computes the aerodynamic loads on the deformed VLM geometry, but the UM/NAST model does not because it uses airfoil properties computed in undeformed shape. As a result, UM/NAST-VLM predicts smaller deflections than UM/NAST at the highest flow speeds, though the impact of this aerodynamic geometrical nonlinearity is small [18].

Tables 2 and 3 compare UM/NAST tip vertical displacements and twist angles at selected conditions showing the percentage differences with respect to the fully nonlinear results. Neglecting follower aerodynamics underestimates tip vertical displacements and twist angles by up to about 10% while neglecting nonlinear kinematics overestimates them by up to about 50%. There is no difference between considering or neglecting follower aerodynamics in the case of linear kinematics. These results show that nonlinear kinematics is the dominant geometrical nonlinearity in the static aeroelastic response.

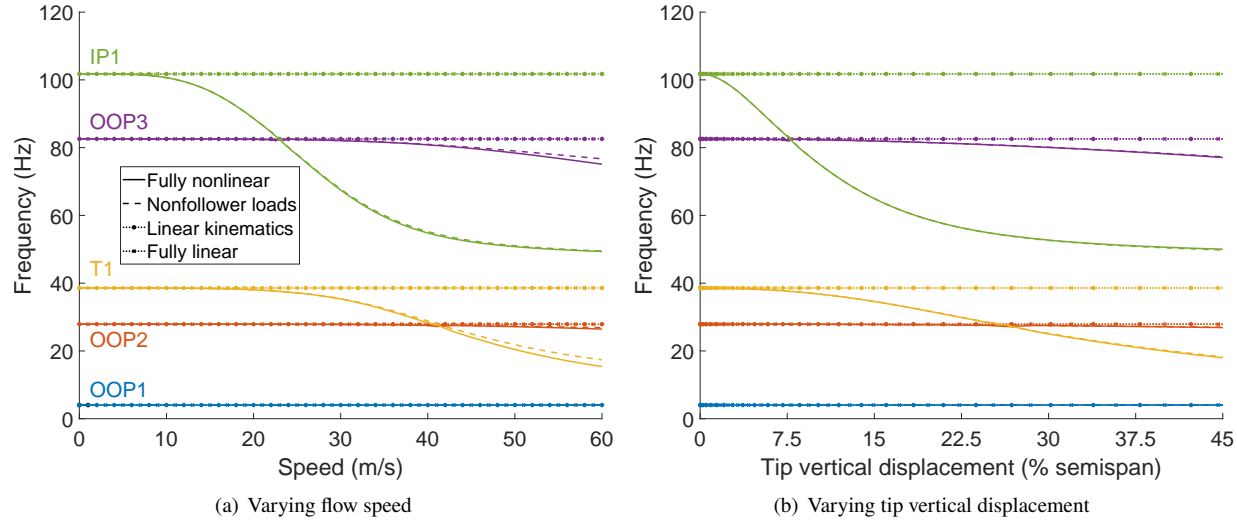


Fig. 8 Pazy wing natural frequencies in deformed shape at $\alpha_r = 7$ deg.

B. Modal Analysis in Deformed Shape

Before studying geometrically nonlinear effects, the UM/NAST fully nonlinear modal analysis in deformed shape is verified with the MSC Nastran nonlinear solver SOL 400 [27]. Each SOL 400 solution computes the static deformed shape of the built-up FEM under frozen aerodynamic loads from converged UM/NAST-VLM solutions followed by a local modal analysis. Figure 7 compares the results from UM/NAST, UM/NAST, and SOL 400 for the Pazy wing without skin (the built-up FEM with skin fails in SOL 400 [8]) at root angle of attack $\alpha_r = 7$ deg. Each natural frequency is in a different color and labeled as its corresponding mode in the undeformed shape (zero flow speed). The solid lines are the results from UM/NAST (beam model coupled with strip theory); the dash-dotted lines are the results from UM/NAST-VLM (beam model coupled with the VLM); the circles are the results from SOL 400 (built-up FEM under frozen UM/NAST-VLM aerodynamic loads).

The UM/NAST and UM/NAST-VLM results overlap, showing that approximating wingtip effects using strip theory does not impact the modal solution. This is in line with the agreement between the static aeroelastic results from the two models discussed in Sec. V.A. The UM/NAST fully nonlinear model captures the overall trend of the natural frequencies of the built-up FEM despite using much fewer DOF. Table 4 quantifies the agreement by comparing natural frequencies for selected flow speeds. The OOP1 frequency is practically constant with the flow speed. Differences in the values predicted by the beam model and by the built-up FEM increase from 0.1% to 1% and arise from the slightly different deformed shapes predicted by the two models at larger deflections [8]. The OOP2 and OOP3 frequencies vary with the flow speed, but the excursion is small and the built-up FEM and beam results differ by less than 1%. The T1 frequency reduces by more than 50% as the flow speed and the tip vertical displacements increase. The beam model underestimates the built-up FEM frequency by up to 15% (see Table 1), though absolute differences are below 2.5 Hz. The beam model also predicts a larger IP1 frequency drop, though differences with the built-up FEM are within 3%.

Next, the discussion shifts to the role of geometrically nonlinear effects for the UM/NAST model with skin later used in the flutter analyses (the models with and without skin show similar trends). Figure 8(a) shows the first five natural frequencies for different geometrically nonlinear effects. Again, frequencies are labeled according to their corresponding mode in the undeformed shape. All frequencies are constant with the flow speed in the case of linear kinematics because the structural equations are linearized about the undeformed shape. With nonlinear kinematics, neglecting follower aerodynamics does not impact the OOP1 frequency and only impacts the OOP2, OOP3, and IP1 frequencies slightly. The most appreciable impacts are on the T1 frequency at flow speeds beyond 40 m/s, where the results with and without follower aerodynamics differ by up to about 13%. The frequencies for the case of follower aerodynamics show a higher decrease with the flow speed due to the larger wing deflections (Sec. V.A.). However, the results with follower and nonfollower aerodynamics overlap when the frequencies are plotted as a function of the tip vertical displacement in Fig. 8(b), with the flow speed as an implicit parameter of the curves. This shows that the modal scenario of a very flexible wing at a given root angle of attack only depends on its deformed shape regardless of the flow speed that produces such shape [28].

Table 4 Pazy wing natural frequencies in deformed shape at $\alpha_r = 7$ deg for selected conditions.

(a) $U = 10$ m/s, tip vertical displacement = 1.50% semispan					(b) $U = 20$ m/s, tip vertical displacement = 6.16% semispan				
SOL 400			UM/NAST		SOL 400			UM/NAST	
#	Mode type	Freq. (Hz)	Freq. (Hz)	Δ (%)	#	Mode type	Freq. (Hz)	Freq. (Hz)	Δ (%)
1	OOP1	4.04	4.05	0.17	1	OOP1	4.04	4.05	0.16
2	OOP2	27.52	27.72	0.73	2	OOP2	27.50	27.70	0.74
3	T1	38.27	38.18	-0.23	3	T1	37.82	37.66	-0.42
4	OOP3	81.07	81.90	1.02	4	OOP3	80.88	81.77	1.11
5	IP1	102.15	102.92	0.75	5	IP1	90.49	89.59	-0.99

(c) $U = 30$ m/s, tip vertical displacement = 14.38% semispan					(d) $U = 40$ m/s, tip vertical displacement = 26.11% semispan				
SOL 400			UM/NAST		SOL 400			UM/NAST	
#	Mode type	Freq. (Hz)	Freq. (Hz)	Δ (%)	#	Mode type	Freq. (Hz)	Freq. (Hz)	Δ (%)
1	OOP1	4.05	4.05	0.14	1	OOP1	4.06	4.06	0.08
2	OOP2	27.42	27.63	0.75	2	OOP2	27.15	27.30	0.54
3	T1	35.50	34.94	-1.58	3	T1	29.46	27.90	-5.27
4	IP1	69.34	67.30	-2.94	4	IP1	56.14	54.36	-3.17
5	OOP3	80.81	81.40	0.73	5	OOP3	79.56	80.13	0.72

(e) $U = 50$ m/s, tip vertical displacement = 39.88% semispan					(f) $U = 60$ m/s, tip vertical displacement = 53.15% semispan				
SOL 400			UM/NAST		SOL 400			UM/NAST	
#	Mode type	Freq. (Hz)	Freq. (Hz)	Δ (%)	#	Mode type	Freq. (Hz)	Freq. (Hz)	Δ (%)
1	OOP1	4.05	4.07	0.46	1	OOP1	4.04	4.09	1.38
2	T1	22.39	20.11	-10.19	2	T1	17.76	15.21	-14.33
3	OOP2	26.83	26.96	0.48	3	OOP2	26.14	26.25	0.42
4	IP1	51.70	50.32	-2.66	4	IP1	50.26	48.90	-2.71
5	OOP3	77.34	77.67	0.43	5	OOP3	74.47	74.38	-0.12

To summarize, neglecting nonlinear kinematics misses the changes in the modal scenario with deformation. Neglecting follower aerodynamics misses the map from operating conditions (flow speed and root angle of attack) to natural frequencies, but the results with and without follower aerodynamics are the same once natural frequencies are plotted as a function of the tip vertical displacement. Follower aerodynamic effects mostly affect the frequency of the torsion-dominated mode at the highest flow speeds, with only slight impacts on the other frequencies.

C. Hump Mode Flutter Boundary in Deformed Shape

This section investigates the impact of geometrically nonlinear effects of the hump mode flutter boundary in the root angle of attack range $\alpha_r = 3 \rightarrow 7$ deg. In this range, the UM/NAST fully nonlinear model captures the experimental flutter onset speeds within 3.5% [9]. The discussion focuses on the results based on nonlinear kinematics with and without follower aerodynamics. The results based on linear kinematics are not shown because the hump mode flutter onset and offset speeds are close to the values in undeformed shape for low deflections, where the hump mode is barely unstable with the current low-order aerodynamic model [9]. Additionally, in the case of linear kinematics, the hump mode is stabilized by the changes in the aerodynamic linearization as deflections increase, showing that nonlinear kinematics is key to capturing this flutter mechanism. The discussion involves only results from UM/NAST due to the lack of higher-order numerical solutions. Differently from Secs. V.A and V.B, the results in this section do not include the tip mass. With the tip mass, the hump mode does not flutter and the wing experiences a hard flutter crossing mechanism [3].

Figure 9 shows the hump mode flutter onset and offset speeds for varying root angle of attack [Fig. 9(a)] or varying tip vertical displacement [Fig. 9(b)]. Figure 9(a) includes markers for the experimental flutter onsets and offsets from forward and reverse flow speed sweeps [4]. The solid curves are the fully nonlinear results (nonlinear kinematics and follower aerodynamics) [9] while the dashed curves are the results for nonfollower aerodynamics. The flutter onset and offset speeds are distinguished using different colors. Figure 9(b) also shows the static equilibrium paths at selected root angles of attack as solid (fully nonlinear) and dashed (nonfollower aerodynamics) thin black lines.

Neglecting follower aerodynamics predicts higher flutter onset and offset speeds at each root angle of attack. Table 5 compares the flutter speeds along with their percentage differences. The flutter onset speeds with and without follower aerodynamics differ by 1.3% to 1.8% as the root angle of attack varies from 3 to 7 deg; the offset speeds differ by 3.7% to 4%. These differences are explained considering that nonfollower aerodynamics causes smaller wing deflections and smaller changes in the frequency of the torsion-dominated mode with flow speed (which drive the hump mode flutter mechanism). These two effects widen the hump mode instability range at each root angle of attack and shift it at higher flow speeds. Differences between the cases with and without follower aerodynamics increase with the strength of follower effects at higher root angle of attack and flow speed. However, follower effects have an overall much smaller impact on the flutter boundary than nonlinear kinematics.

Table 6 compares the tip vertical displacements at the hump mode flutter onset and offset speeds. As Fig. 9(b) shows, flutter occurs at about the same tip vertical displacement with and without follower aerodynamics (differences remain about 0.5–0.7% as the root angle of attack increases). The tip vertical displacements at the flutter offset speeds with and without follower aerodynamics differ by about 4% but follow a similar trend. The flutter frequencies with and without follower aerodynamics are practically the same (Table 7). Differences remain below 1% for most of the flutter boundary, with slightly larger values of 1.5–2% only for the flutter frequencies at offset speeds for the highest roots angle of attack.

To complete the discussion, Fig. 10 shows root loci for $U = 0 \rightarrow 100$ m/s at $\alpha_r = 3, 5, 7$ deg. The aeroelastic eigenvalues with and without follower aerodynamics evolve along the same curves but achieve different values for each combination of flow speed and root angle of attack due to the different deformed shapes. These results highlight that the stability scenario of a very flexible wing at a given root angle of attack is driven by the deformation level, and the aeroelastic frequencies and damping values collapse onto the same curves when presented with the flow speed as an implicit parameter (such as in the root locus visualization of Fig. 10 or, alternatively, in frequency and damping diagrams with respect to the tip vertical displacement instead of the flow speed).

In summary, the hump mode flutter boundary is driven by nonlinear kinematics through the changes in the wing modal characteristics with static deflection, specifically, the reduced frequency separation between the structural modes that are originally the T1 and OOP2 modes in undeformed shape. Neglecting follower aerodynamics overestimates the flutter onset and offset speeds by up to 4% and predicts a wider hump mode instability region. However, follower aerodynamics effects do not practically impact the flutter frequency nor change any qualitative trends for this wing.

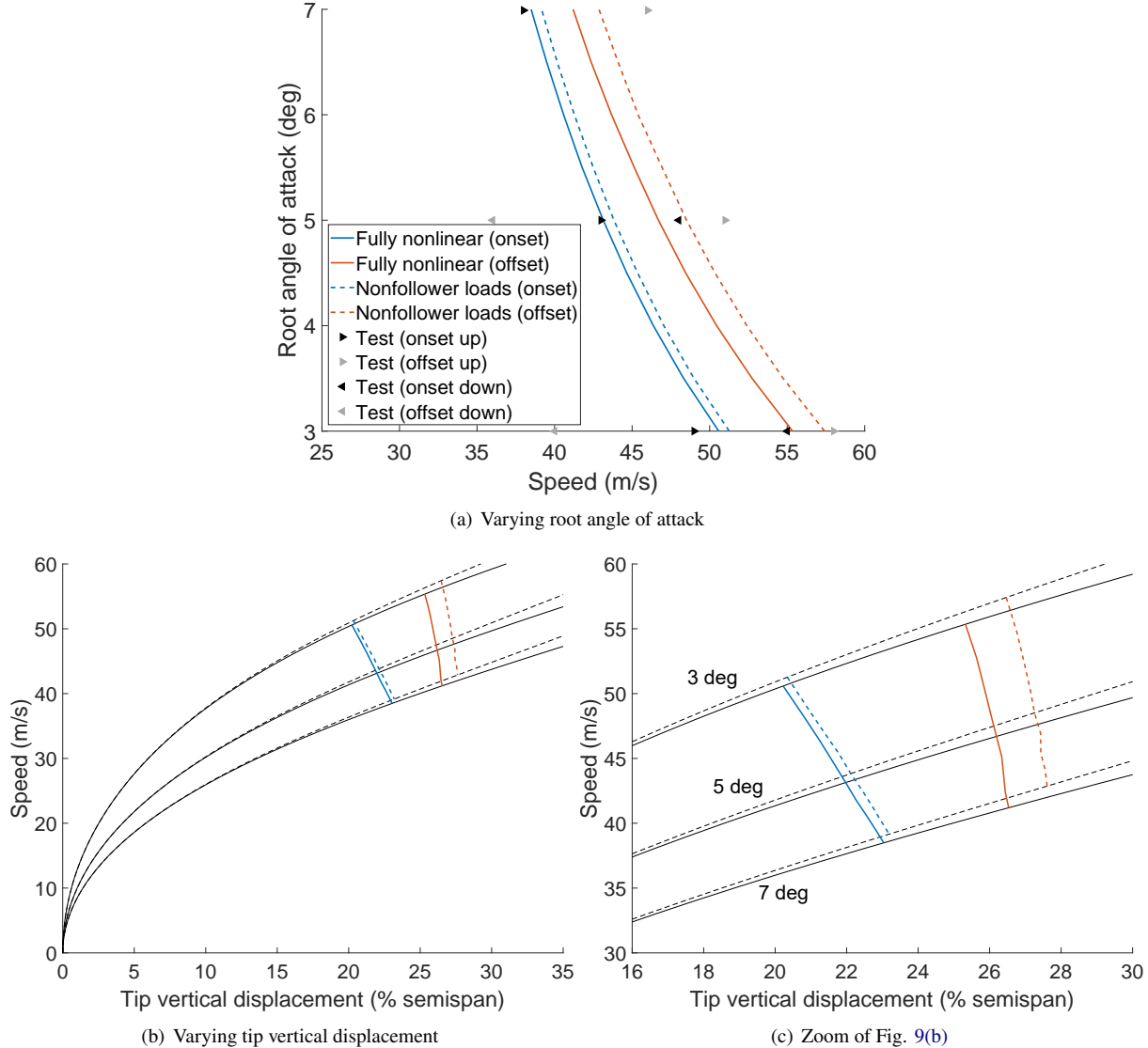


Fig. 9 Pazy wing hump mode flutter boundary.

Table 5 Pazy wing hump mode flutter onset and offset speeds (m/s).

α_r (deg)	Onset speed			Offset speed		
	Fully nonlinear	Nonfollower loads	Δ (%)	Fully nonlinear	Nonfollower loads	Δ (%)
3.0	50.58	51.26	1.34	55.35	57.41	3.73
3.5	48.32	48.99	1.38	52.74	54.74	3.80
4.0	46.37	47.04	1.45	50.45	52.40	3.86
4.5	44.65	45.36	1.58	48.45	50.34	3.91
5.0	43.14	43.83	1.60	46.70	48.51	3.89
5.5	41.78	42.49	1.71	45.14	46.93	3.98
6.0	40.58	41.28	1.71	43.68	45.39	3.92
6.5	39.49	40.17	1.72	42.36	44.09	4.10
7.0	38.49	39.16	1.75	41.19	42.86	4.05

Table 6 Pazy wing hump mode tip vertical displacements (% semispan) at the flutter onset and offset speeds.

α_r (deg)	Tip vertical displacement at onset speed			Tip vertical displacement at offset speed		
	Fully nonlinear	Nonfollower loads	Δ (%)	Fully nonlinear	Nonfollower loads	Δ (%)
3.0	20.22	20.34	0.57	25.32	26.46	4.50
3.5	20.78	20.88	0.49	25.64	26.76	4.38
4.0	21.25	21.36	0.53	25.85	26.97	4.32
4.5	21.63	21.79	0.70	26.03	27.13	4.25
5.0	21.97	22.12	0.65	26.19	27.26	4.07
5.5	22.27	22.44	0.80	26.34	27.43	4.13
6.0	22.56	22.72	0.73	26.39	27.43	3.94
6.5	22.81	22.96	0.66	26.44	27.56	4.22
7.0	23.04	23.19	0.66	26.53	27.61	4.05

Table 7 Pazy wing hump mode flutter frequencies (Hz) at the flutter onset and offset speeds.

α_r (deg)	Frequency at onset speed			Frequency at offset speed		
	Fully nonlinear	Nonfollower loads	Δ (%)	Fully nonlinear	Nonfollower loads	Δ (%)
3.0	30.51	30.74	0.77	28.12	28.08	-0.15
3.5	30.36	30.61	0.82	28.07	28.03	-0.12
4.0	30.23	30.48	0.85	28.04	28.02	-0.10
4.5	30.12	30.37	0.84	28.02	28.00	-0.08
5.0	30.01	30.28	0.90	28.00	27.99	-0.01
5.5	29.93	30.19	0.86	27.98	27.96	-0.06
6.0	29.84	30.10	0.88	27.34	27.99	2.38
6.5	29.75	30.02	0.92	27.47	27.77	1.10
7.0	29.68	29.95	0.93	27.60	27.18	-1.54

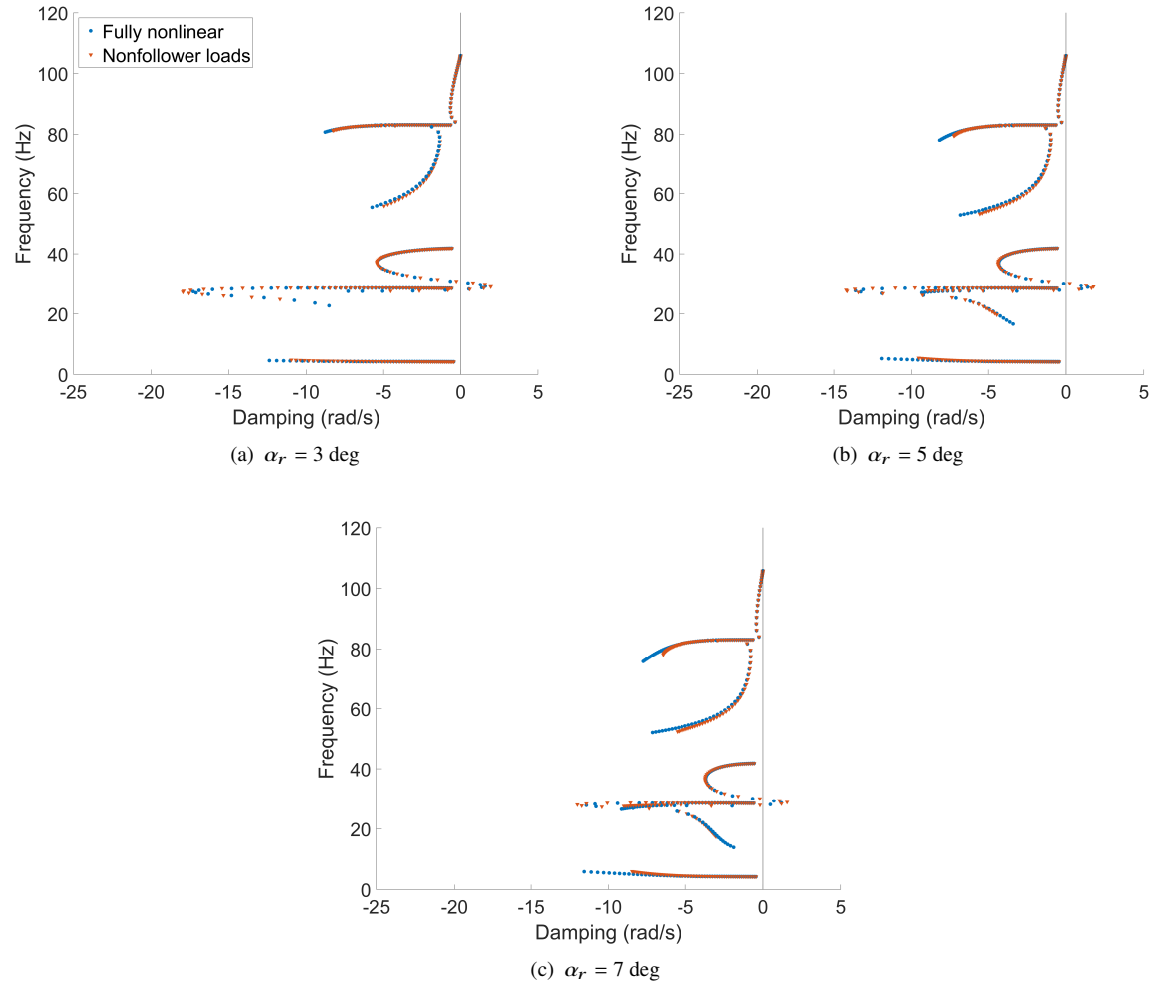


Fig. 10 Pazy wing root loci for $U = 0 \rightarrow 100 \text{ m/s}$ at $\alpha_r = 3, 5, 7 \text{ deg}$.

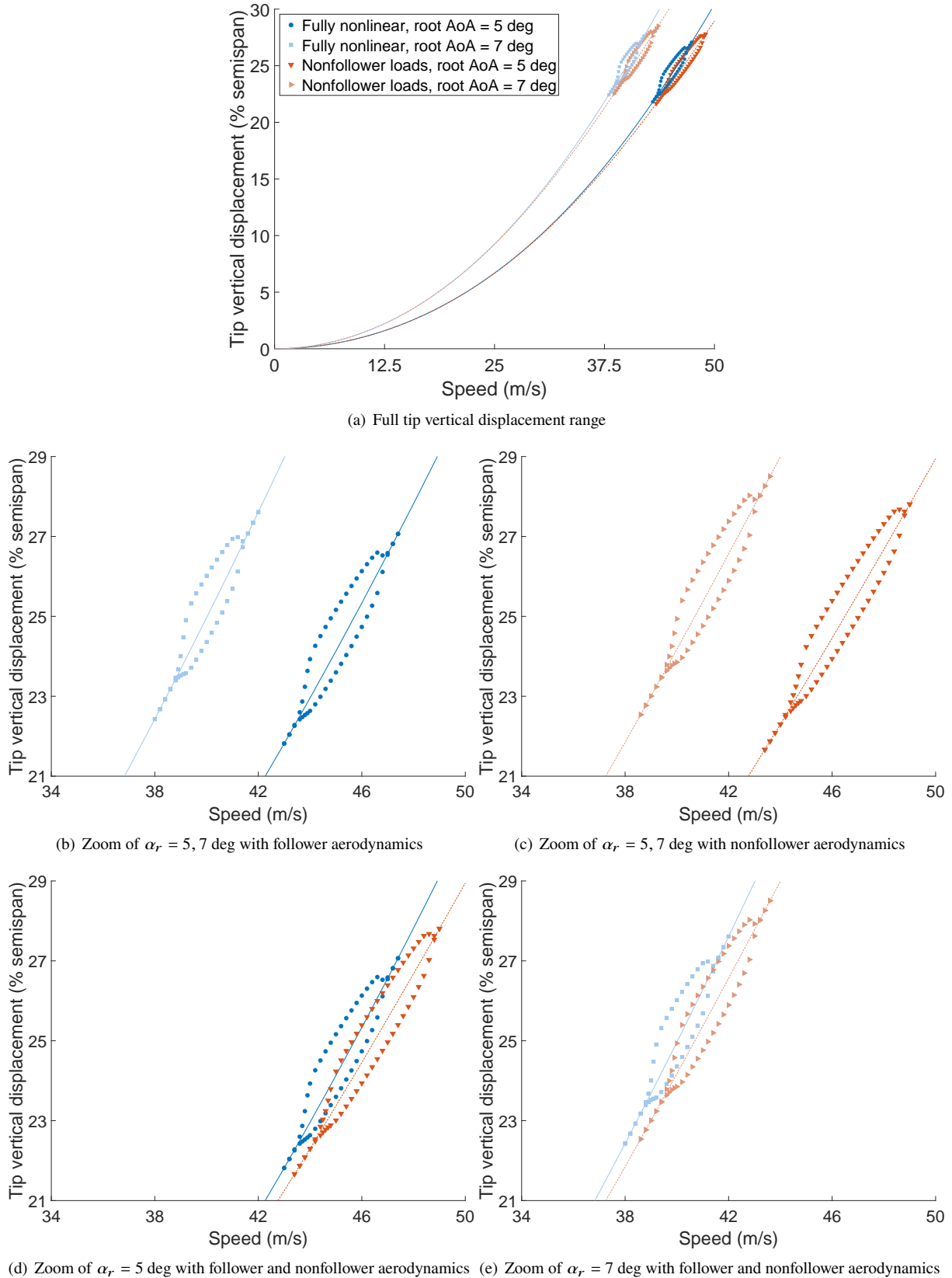


Fig. 11 Pazy wing hump mode bifurcation diagram at $\alpha_r = 5, 7$ deg.

D. Post-Flutter Dynamics

To conclude, this section analyzes the impact of follower aerodynamics on the hump mode post-flutter dynamics at $\alpha_r = 5, 7$ deg. The post-flutter dynamics is characterized by extracting the tip maximum and minimum displacements at the end of transient responses at different flow speeds. The transient responses involve perturbing the static deformed shape by applying a unit tip force at the beginning of each simulation. Again, the discussion involves only results from UM/NAST due to the lack of higher-order numerical solutions.

Figure 11(a) shows the bifurcation diagrams along with the static equilibrium paths (thin solid and dashed lines). The results with and without follower aerodynamics and at the two root angles of attack are denoted by different colors and markers, with higher root angles of attack in lighter shades. The bifurcation diagrams with and without follower aerodynamics are supercritical at both root angles of attack, as highlighted by the zooms in Figs. 11(a) to 11(d). These results confirm that capturing the experimentally observed subcritical behavior associated with the Pazy wing hump mode requires aerodynamic nonlinear effects such as stall [9]. The flutter onset and offset speeds estimated from the transient responses are within 0.5 m/s of the results in Sec. V.C obtained from eigenvalue analyses. These slight differences are attributed to numerical damping in the time-marching scheme and to the long transients required to fully develop a self-sustained oscillation or to recover to the initial equilibrium close to the flutter boundary. Neglecting follower aerodynamics mainly shifts the bifurcation diagram at higher flow speeds while making it wider. This is because of the impact of follower aerodynamics on the hump mode flutter boundary discussed in Sec. V.C. The bifurcation diagrams with and without follower aerodynamics are qualitatively similar and lie in approximately the same tip vertical displacement range of 22–28% semispan. Most of the tip vertical displacement is associated with the static aeroelastic response, with dynamic oscillations limited to 1–2% semispan. The slight impact of follower aerodynamics on the amplitude of the post-flutter dynamics is attributed to the small dynamic excursions about the static deformed shape, which translate to small changes in aerodynamic load orientation with respect to equilibrium.

In summary, follower aerodynamic loads shift and shrink the hump mode bifurcation diagram due to the lower flutter onset and offset speeds, but do not change qualitative trends for this wing. The low-order aeroelastic model including only geometrical nonlinearities predicts a supercritical behavior in place of the experimentally observed subcritical bifurcation [3, 9].

VI. Concluding Remarks

This paper investigated geometrically nonlinear effects in the aeroelastic behavior of a very flexible wing in low-speed flow using the Pazy wing as a representative test case. The study leveraged a verified and validated low-order model that consists of a geometrically nonlinear beam coupled with potential flow thin airfoil aerodynamics. The complete model was implemented into the University of Michigan's Nonlinear Aeroelastic Simulation Toolbox, a low-order multidisciplinary framework for studying very flexible wings and aircraft that can consider geometrical nonlinearities associated with nonlinear kinematics and follower aerodynamic loads individually or in combination.

The results showed that nonlinear kinematics is the primary nonlinearity in the Pazy wing static aeroelastic response, natural frequencies in deformed shape, and hump mode flutter boundary. Neglecting follower aerodynamics underestimates tip vertical displacements by up to 10%, consequently affecting the natural frequencies and hump mode flutter onset and offset speeds. However, there is no qualitative change in the results with and without follower aerodynamics: the natural frequencies and aeroelastic eigenvalues at a given root angle of attack evolve along the same curves once plotted with respect to the tip vertical displacement, with the flow speed as an implicit parameter, or in a root locus. The only impact of follower aerodynamics on the bifurcation diagram is in shifting and stretching its flow speed bounds due to the different flutter onset and offset speeds. There is no change in the predicted bifurcation behavior nor in the amplitude of post-flutter dynamics for the analyzed wing and flutter mechanism.

Acknowledgments

The authors thank Prof. Daniella Raveh and Ariel Drachinsky (Technion) for sharing numerical and experimental data that supported assessing the model used in this work. The authors also thank Dr. Markus Ritter (German Aerospace Center) for coordinating the activities of the AePW3-LDWG.

References

- [1] Afonso, F., Vale, J., Oliveira, É., Lau, F., and Suleman, A., "A Review on Non-Linear Aeroelasticity of High Aspect-Ratio Wings," *Progress in Aerospace Sciences*, Vol. 89, 2017, pp. 40–57. <https://doi.org/10.1016/j.paerosci.2016.12.004>.
- [2] Cesnik, C. E. S., Palacios, R., and Reichenbach, E. Y., "Reexamined Structural Design Procedures for Very Flexible Aircraft," *Journal of Aircraft*, Vol. 51, No. 5, 2014, pp. 1580–1591. <https://doi.org/10.2514/1.C032464>.
- [3] Avin, O., Raveh, D. E., Drachinsky, A., Ben-Shmuel, Y., and Tur, M., "Experimental Aeroelastic Benchmark of a Very Flexible Wing," *AIAA Journal*, 2022, pp. 1–24. <https://doi.org/10.2514/1.J060621>, article in advance.
- [4] Drachinsky, A., Avin, O., Raveh, D. E., Ben-Shmuel, Y., and Tur, M., "Flutter Tests of the Pazy Wing," *AIAA Journal*, 2022, pp. 1–8. <https://doi.org/10.2514/1.J061717>, article in advance.
- [5] Drachinsky, A., and Raveh, D. E., "Nonlinear Aeroelastic Analysis of Highly Flexible Wings using the Modal Rotation Method," *AIAA Journal*, 2022, pp. 1–13. <https://doi.org/10.2514/1.j061065>, article in advance.
- [6] Goizueta, N., Wynn, A., Palacios, R., Drachinsky, A., and Raveh, D. E., "Flutter Predictions for Very Flexible Wing Wind Tunnel Test," *Journal of Aircraft*, 2022, pp. 1–16. <https://doi.org/10.2514/1.C036710>, article in advance.
- [7] Riso, C., and Cesnik, C. E. S., "Correlations Between UM/NAST Nonlinear Aeroelastic Simulations and the Pre-Pazy Wing Experiment," *AIAA SciTech Forum*, Online, 2021, pp. 1–24. <https://doi.org/10.2514/6.2021-1712>, AIAA-2021-1712.
- [8] Riso, C., and Cesnik, C. E. S., "Low-Order Geometrically Nonlinear Aeroelastic Modeling and Analysis of the Pazy Wing Experiment," *AIAA SciTech Forum*, San Diego, CA and Online, 2022, pp. 1–30. <https://doi.org/10.2514/6.2022-231>, AIAA-2022-231.
- [9] Riso, C., and Cesnik, C. E. S., "Post-Flutter Dynamics of the Pazy Wing Geometrically Nonlinear Benchmark Model," *International Forum on Aeroelasticity and Structural Dynamics*, Madrid, Spain, 2022, pp. 1–18. IFASD-2022-073.
- [10] Ritter, M., Hilger, J., and Zimmer, M., "Static and Dynamic Simulations of the Pazy Wing Aeroelastic Benchmark by Nonlinear Potential Aerodynamics and Detailed FE Model," *2021 AIAA SciTech Forum*, 2021, pp. 1–16. <https://doi.org/10.2514/6.2021-1713>, AIAA-2021-1713.
- [11] Ritter, M., and Hilger, J., "Dynamic Aeroelastic Simulations of the Pazy Wing by UVLM with Nonlinear Viscous Corrections," *2022 AIAA SciTech Forum*, San Diego, CA and Online, 2022, pp. 1–18. <https://doi.org/10.2514/6.2022-0177>, AIAA-2022-0177.
- [12] Mertens, C., Costa, J. L., Sodja, J., Sciacchitano, A., and van Oudheusden, B. W., "Integrated Aeroelastic Measurements of the Periodic Gust Response of a Highly Flexible Wing," *International Forum on Aeroelasticity and Structural Dynamics*, Madrid, Spain, 2022, pp. 1–21. IFASD-2022-132.
- [13] Artola, M., Goizueta, N., Wynn, A., and Palacios, R., "Aeroelastic Control and Estimation with a Minimal Nonlinear Modal Description," *AIAA Journal*, Vol. 59, No. 7, 2021, pp. 2697–2713. <https://doi.org/10.2514/1.j060018>.
- [14] Goizueta, N., Wynn, A., and Palacios, R., "Fast Flutter Evaluation of Very Flexible Wing using Interpolation on an Optimal Training Dataset," *2022 AIAA SciTech Forum*, San Diego, CA and Online, 2022, pp. 1–21. <https://doi.org/10.2514/6.2022-1345>, AIAA-2022-1345.
- [15] Righi, M., "Uncertainty Quantification in Flutter Prediction of a Wind Tunnel Model Exhibiting Large Displacements," *2021 AIAA SciTech Forum*, Virtual Event, 2021, pp. 1–9. <https://doi.org/10.2514/6.2021-1037>, AIAA-2021-1037.
- [16] Righi, M., Carnevali, L., and Ravasi, M., "Uncertainties Quantification in Flutter Prediction of a Wind Tunnel Model Exhibiting Large Displacements," *2022 AIAA SciTech Forum*, San Diego, CA and Online, 2022, pp. 1–10. <https://doi.org/10.2514/6.2022-0178>, AIAA-2022-0178.
- [17] Dowell, E., Edwards, J., and Strganac, T., "Nonlinear Aeroelasticity," *Journal of Aircraft*, Vol. 40, No. 5, 2003, pp. 857–874. <https://doi.org/10.2514/2.6876>.
- [18] Patil, M. J., and Hodges, D. H., "On the Importance of Aerodynamic and Structural Geometrical Nonlinearities in Aeroelastic Behavior of High-Aspect-Ratio Wings," *Journal of Fluids and Structures*, Vol. 19, No. 7, 2004, pp. 905–915. <https://doi.org/10.1016/j.jfluidstructs.2004.04.012>.
- [19] Su, W., and Cesnik, C. E. S., "Strain-Based Geometrically Nonlinear Beam Formulation for Modeling Very Flexible Aircraft," *International Journal of Solids and Structures*, Vol. 48, No. 16–17, 2011, pp. 2349–2360. <https://doi.org/10.1016/j.ijsolstr.2011.04.012>.

- [20] Peters, D. A., Hsieh, M. C. A., and Torrero, A., "A State-Space Airloads Theory for Flexible Airfoils," *Journal of the American Helicopter Society*, Vol. 52, No. 4, 2007, pp. 329–342. <https://doi.org/10.4050/JAHS.52.329>.
- [21] Su, W., and Cesnik, C. E. S., "Nonlinear Aeroelasticity of a Very Flexible Blended-Wing-Body Aircraft," *Journal of Aircraft*, Vol. 47, No. 5, 2010, pp. 1539–1553. <https://doi.org/10.2514/1.47317>.
- [22] Su, W., "Coupled Nonlinear Aeroelasticity and Flight Dynamics of Fully Flexible Aircraft," PhD Thesis, University of Michigan, Ann Arbor, MI, 2008.
- [23] Howcroft, C., Cook, R., Calderon, D., Lambert, L., Castellani, M., Cooper, J. E., Lowenberg, M. H., Neild, S. A., and Coetze, E., "Aeroelastic Modelling of Highly Flexible Wings," *15th Dynamics Specialists Conference*, San Diego, CA, 2016, pp. 1–26. <https://doi.org/10.2514/6.2016-1798>, AIAA-2016-1798.
- [24] Anon., *MSC Nastran Aeroelastic Analysis User's Guide*, 2017.
- [25] Riso, C., Sanghi, D., Cesnik, C. E. S., Vetrano, F., and Teufel, P., "Parametric Roll Maneuverability Analysis of a High-Aspect-Ratio-Wing Civil Transport Aircraft," *AIAA SciTech Forum*, Orlando, FL, 2020, pp. 1–23. <https://doi.org/10.2514/6.2020-1191>, AIAA-2020-1191.
- [26] Anon., *ZAERO Theoretical Manual Version 9.2*, 2017.
- [27] Anon., *MSC Nastran Non Linear User's Guide SOL400*, 2016.
- [28] Patil, M. J., Hodges, D. H., and Cesnik, C. E. S., "Limit-Cycle Oscillations in High-Aspect-Ratio Wings," *Journal of Fluids and Structures*, Vol. 15, No. 1, 2001, pp. 107–132. <https://doi.org/10.1006/jfls.2000.0329>.